

Mathematical Modelling of Engineering Problems

Vol. 12, No. 10, October, 2025, pp. 3627-3635

Journal homepage: http://iieta.org/journals/mmep

Equivalent Damping Matrix for Perforated Circular Thin Plates Using Galerkin Approach

Check for updates

Tahseen Taha Othman^{1*}, Mohammed Taha Yassin², Yusra Abdullah Jasim²

- ¹ Petroleum Control Systems Engineering, Tikrit University, Tikrit 34001, Iraq
- ² Mechanical Engineering Department, Tikrit University, Tikrit 34001, Iraq

Corresponding Author Email: tahseentaha@tu.edu.iq

Copyright: ©2025 The authors. This article is published by IIETA and is licensed under the CC BY 4.0 license (http://creativecommons.org/licenses/by/4.0/).

https://doi.org/10.18280/mmep.121026

Received: 16 May 2025 Revised: 11 August 2025 Accepted: 12 September 2025 Available online: 31 October 2025

Keywords:

equivalent damping matrix, perforated circular plate, ligament efficiency, Galerkin method

ABSTRACT

An equivalent damping matrix for circular perforated plates with square and rectangular penetration patterns was developed in this study. Galerkin approaches via eigenfunctions of the solid plate as trial functions were used to derive the plate's mass matrix and stiffness matrix. A solid plate replaced the perforated plate using the equivalent material properties concept. The proportional damping principle was used to construct the equivalent damping matrix. The first four damping ratios associated with the first four natural frequencies were measured experimentally and used to determine the proportionality constants. Two ligament efficiencies were assessed for each penetration pattern by varying hole diameters while keeping the width of the partition between holes constant. A comparison of the first four natural frequencies between experimental and analytical results shows that a good result can be achieved when the eigenfunctions of a solid circular plate are used as trial functions in the Galerkin approach. Using an equivalent damping matrix decreases the percentage difference between them by 0.1% for the first mode, 4.9% for the second mode, 4.1% for the third mode, and 3.4% for the fourth mode.

1. INTRODUCTION

The dynamic characteristics of perforated plates have been studied by many authors since they have many engineering applications. Among these applications are nuclear reactors and tube sheet heat exchangers, and combustion chambers [1]. They provide both a flow passage for fluid and structural support. A circular perforated plate is one type of these plates. The holes could be circular or square. There are two types of perforation patterns: square patterns (Figure 1) and triangular patterns (Figure 2).

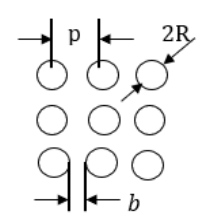


Figure 1. Square penetration pattern

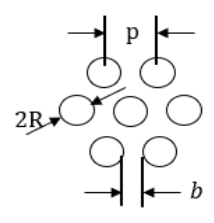


Figure 2. Triangular penetration pattern

The main dimensionless parameter for perforated plates is the ligament efficiency η , which can be defined as:

$$\eta = \frac{b}{p}$$

where, p is the pitch and b is the minimum ligament width. It is worth mentioning that the different values of η can be achieved in two ways: 1)- keeping the pitch constant and changing the radius of holes, and 2)- vice versa. The first one is approved in this study.

A fundamental frequency of a rectangular perforated plate is determined by Mali and Singru [2], by considering the holes as concentrated negative mass, while the perforated plate was considered a plate with uniformly distributed mass.

Validation with FEM shows that the analytical model is proper for obtaining the fundamental frequency for small perforations.

Besides, FEM was used to study the effect of adding micro holes to rectangular plates with macro holes on their natural frequency and mode shape [3]. Cunningham et al. [4] provided the dynamic finite element model to predict the effect of perforations on the natural frequency of clamped circular flat plates. The impact of the circular hole's diameter and position on the natural frequencies of the rectangular plate was examined by Jamali et al. [5] through both experimental and analytical methods using finite element modeling. In contrast, the Simula Abaqus software was used to investigate the dynamic characteristics of perforated plates with holes of complex geometry [6]. A numerical model introduced by

Zhang et al. [7] to study the vibrational properties of the braided fiber reinforced composite rotating plates with holes.

Recently, many researchers have focused on vibration analysis of solid plates made from functionally graded materials (FGM) due to their exceptional thermal properties. After that, the perforation was introduced by Prasshanth et al. [8] to study the effect of plate thickness, number of perforations, and penetration diameters on the dynamic characteristics of partially perforated circular functionally graded plates, where ANSYS Workbench was used in this investigation.

The drawbacks of the finite element method in this field are very costly and time-consuming. For this reason, many authors focus on using equivalent solid material concepts. In this concept, the perforated plate is replaced by a solid plate with equivalent elastic constants, which behaves similarly to a perforated plate when subjected to the same load conditions. By equating the average strains in the perforated plate material to those in an equivalent solid material, the effective elastic constant for thick perforated plates was determined by Slot and O'Donnell [9]. The concept was developed by O'Donnell [10] to include those of thin perforated plates. However, this concept is valid for the first mode from a modal characteristic point of view [11].

The more efficient equivalent material properties of a square and triangular perforated plate can be used for a vibration analysis as a function of ligament efficiency, as suggested by Jhung and Jo [12], and this can be done regardless of the plate's thickness. An alternative approach to obtaining an expression for equivalent elastic properties for rectangular perforated plates is provided by Jhung and Jeong [13]. The formulation was based on Rayleigh's quotient, and fundamental natural frequency was obtained experimentally. On the other hand, the geometric nonlinearity of the circular perforated plate was considered by Ehrhardt et al. [14]. In this study, the nonlinear normal modes were measured experimentally and compared with those obtained numerically. Due to the wide use of partially perforated circular plates (perforation was at the central region of the plate) in reactor internals, it was also developed from a vibration point of view by Jeong and Jhung [15] using finite element analysis. The results were compared with the analytical method based on the Rayleigh-Ritz. The study divided the partially circular perforated plates into a perforated central region and a solid annular region to determine the total kinetic and maximum potential energy. Finally, the modal analysis of the perforated circular plates with a triangular hole pattern was used to extract the effective modulus of elasticity and effective Poisson's ratio by Jeong et al. [16].

All these studies lack consideration for the internal damping effect on the dynamic characteristics of circular perforated plates. Due to a mismatch between the theoretical and experimental values of natural frequencies, the authors of this study developed the equivalent damping matrix using the proportional damping principle. The Mass and stiffness matrix of the perforated plate were determined using exact eigenfunctions of the solid plate as a trial function in the Galerkin method. The effects of internal plate material damping on the first four natural frequencies of the fixed-edge circular solid and perforated plate were studied. Triangular and square penetration patterns with two ligament efficiency η (0.5, 0.75) per pattern were considered. The analytical results were compared with an experimental modal test designed for this purpose.

2. MATHEMATICAL MODELLING

2.1 Free vibration analysis of a solid circular plate

Figure 3 shows a fixed edge circular plate of radius a and thickness h that vibrates transversely perpendicular to the x-y plane. Under the following assumptions: 1)- the plate material is isotropic, 2)- homogeneous, 3)- the plate is so thin that the rotary inertia can be neglected, the partial differential equation of the undamped bending vibration of the circular plate in polar coordinates can be written as

$$D\nabla^4 w(r,\theta,t) + \rho_P h \ddot{w}(r,\theta,t) = 0 \tag{1}$$

where, ∇^4 is bi-harmonic operator and

$$\nabla^2 = \frac{\partial^2}{\partial r^2} + \frac{1}{r} \frac{\partial}{\partial r} + \frac{1}{r^2} \frac{\partial^2}{\partial \theta^2}$$

Is two dimensional Laplacian, in polar coordinates, $w(r, \theta, t)$ is the deflection of a point whose coordinates are (r, θ) at the middle plane of the plate at any time t, $D = E h^3/12(1-v^2)$ is the flexural rigidity of the plate, E is the modulus of elasticity, v is passion's ratio and ρ_p is mass density per unit area.

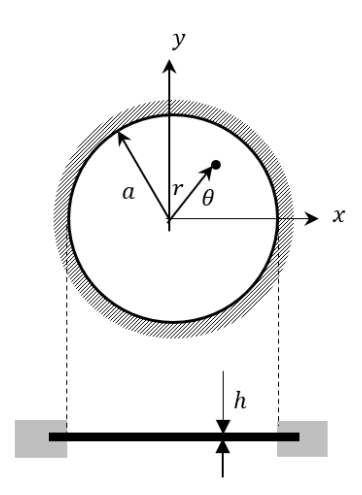


Figure 3. Fixed edge circular plate

2.2 Galerkin approach

The eigenvalue problem in the Galerkin approach is derived by setting the integrated weighted error equal to zero. The Galerkin approach was used in this study because it deals with non-conservative systems, such as systems with internal plate material damping (problem in hand).

In the Galerkin approach, the solution of the plate is assumed in the form:

$$w(r,\theta) = \sum_{i=1}^{n} \alpha_i W_i(r,\theta)$$
 (2)

where, α_i are undetermined coefficients, $W_i(r, \theta)$ are trial comparison (satisfies all boundary conditions) functions and n is the number of trial functions.

Substituting for the approximate series solution (2) into Eq. (1) yields

$$D\sum_{i=1}^{n} \alpha_i \nabla^2 \nabla^2 W_i(r,\theta) + \rho_P h \omega^2 \sum_{i=1}^{n} \alpha_i W_i(r,\theta)$$
 (3)

Multiplying Eq. (3) by the weighting function $\phi_i(r,\theta)$, then equating the integrated result to zero, the Galerkin equation for circular plate vibration can be written as:

$$\iint_{A} \left(D \sum_{i=1}^{n} \alpha_{i} \nabla^{2} \nabla^{2} W_{i}(r, \theta) + \rho_{P} h \omega^{2} \sum_{i=1}^{n} \alpha_{i} W_{i}(r, \theta) \right) \phi_{j}(r, \theta) r dr d\theta = 0,$$

$$i = 1, 2, \dots$$
(4)

where,

$$= \left(\frac{\partial^2}{\partial r^2} + \frac{1}{r}\frac{\partial}{\partial r} + \frac{1}{r^2}\frac{\partial^2}{\partial \theta^2}\right) \left(\frac{\partial^2 W}{\partial r^2} + \frac{1}{r}\frac{\partial W}{\partial r} + \frac{1}{r^2}\frac{\partial^2 W}{\partial \theta^2}\right)$$

or in the expanded form

$$\begin{split} \nabla^4 W(r,\theta,t) &= \frac{\partial^4 W}{\partial r^4} + \frac{2}{r} \frac{\partial^3 W}{\partial r^3} - \frac{1}{r^2} \frac{\partial^2 W}{\partial r^2} + \frac{1}{r^3} \frac{\partial W}{\partial r} \\ &+ \frac{2}{r^2} \frac{\partial^4 W}{\partial r^2 \partial \theta^2} - \frac{2}{r^3} \frac{\partial^3 W}{\partial \theta^2 \partial r} + \frac{4}{r^4} \frac{\partial^2 W}{\partial \theta^2} + \frac{1}{r^4} \frac{\partial^4 W}{\partial \theta^4} \end{split}$$

It should be noted that the weighting function $\phi_i(r,\theta)$ and trail function $W_i(r,\theta)$ are the same in the Galerkin approach [17].

2.3 Derivation of trial function $W_i(r, \theta)$

The eigenfunctions of the solid circular plate were used as a trial function $W_i(r,\theta)$. Since the eigenfunctions (mode shape) are an exact solution of the given boundary value problem, then from Eq. (4), the derived functions will be orthogonal with the function in bracket in Eq. (4).

The eigenvalues of a plate can be deduced as follows: the deflection w can be considered to be separable in space and time as

$$w(r,\theta,t) = W(r,\theta)e^{-j\omega t}$$
 (5)

Substituting Eq. (5) into Eq. (1), the equivalent factorised form is

$$(\nabla^2 + \beta^2)(\nabla^2 - \beta^2) W(r, \theta) = 0 \tag{6}$$

where,

$$\beta^4 = \omega^2 \rho_P h / D \tag{7}$$

and ω is radial frequency.

By separating the function $W(r, \theta)$ into $F(r)G(\theta)$, i.e.,

$$W(r,\theta) = F(r)G(\theta) \tag{8}$$

After some mathematical operations, as carried out in Appendix A, the function $W(r, \theta)$ can be deduced as

$$W(r,\theta) = \left[C_1 J_k(\beta r) + C_3 I_k(\beta r)\right] A \cos k(\theta) \tag{9}$$

where, k is constant and equal to (1, 2, ...), since $G(\theta)$ must be periodic with period 2π [18].

The two boundary conditions of the clamped-edge circular plate were:

$$|w(r)|_{r=a} = \frac{dw(r)}{dr}\bigg|_{r=a} = 0$$

Using Eq. (9), leads to

$$C_1 J_k(\beta a) + C_3 I_k(\beta a) = 0 \tag{10}$$

$$C_1 J_k'(\beta a) + C_3 I_k'(\beta a) = 0 \tag{11}$$

The frequency equation can be deduced as (see Appendix B for Bessel function identities):

$$J_k(\beta a)I_{k+1}(\beta a) + J_{k+1}(\beta a)I_k(\beta a) = 0$$
 (12)

For each value of k, there is an infinite number of roots. The frequency parameter

$$\lambda_{km} = \beta_{km} a$$

Then, from Eq. (7), the natural frequency of the solid plate can be obtained as

$$\omega_{km} = \left(\frac{\lambda_{km}}{a}\right)^2 \sqrt{\frac{D}{\rho_P h}} \tag{13}$$

Maple computer software was used to determine the roots of Eq. (12). Figure 4 shows the first two roots at k = 2.

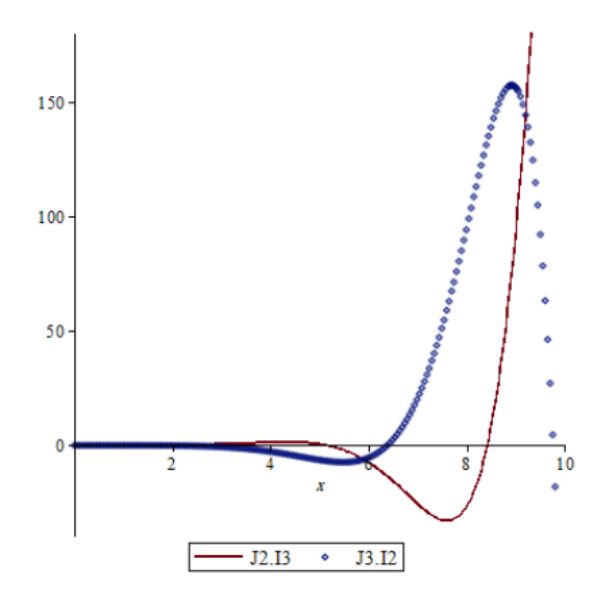


Figure 4. First two roots of Eq. (12) at k = 2

Then, eliminating the constant C_3 from Eq. (10) and substituting it into Eq. (9), the normal modes (trial functions) of the circular plate are reduced to

$$W_{km}(r,\theta) = A_{km} \left[J_k(\beta_{km}r) - \frac{J_k(\beta_{km}a)}{I_k(\beta_{km}a)} I_k(\beta_{km}r) \right] \begin{pmatrix} \sin k\theta \\ \cos k\theta \end{pmatrix}$$
(14)

where, A_{km} is constant for normalization.

Figures 5-8 depict the first four normal modes associated with k,m = 01,11,21,02, respectively (k refers to the order of Bessel's function and m refers to the root number). Two notes can be pointed out from these modes: 1) The mode shapes (Eq. (14)) do not depend on the material of the plate. 2)- The axisymmetric modes correspond to zero order of Bessel's function, while otherwise correspond to asymmetric modes. Eq. (14) represents the trial or weight functions used in Eq. (4) to derive the mass and stiffness matrices. Up to four derivatives of Bessel's functions are given in Appendix B [19].

2.4 Equivalent solid plate

The perforated plate was replaced with an equivalent solid plate that considers the weakening effect of perforation. This can be done by using an equivalent elastic E^* as a function of ligament efficiency η . Because equivalent elastic constant proposed by O'Donnell [10] is not suitable for a modal analysis, Jhung and Jo [12] performed several finite element analyses to suggest an equivalent elastic constant of perforated plates that can be used for a dynamic analysis propose as follows

$$\frac{E^*}{E} = 0.6106 + 1.1253\eta - 2.7118\eta^2
+4.0812\eta^3 - 2.1128\eta^4 (triangular)$$
(15)

$$\frac{E^*}{E} = 0.5280 + 2.0035\eta - 5.4758\eta^2 +7.7474\eta^3 - 3.8968\eta^4 \text{(square)}$$
(16)

Eqs. (15) and (16) can be used for the modal analysis of the entire thickness range of the plate.

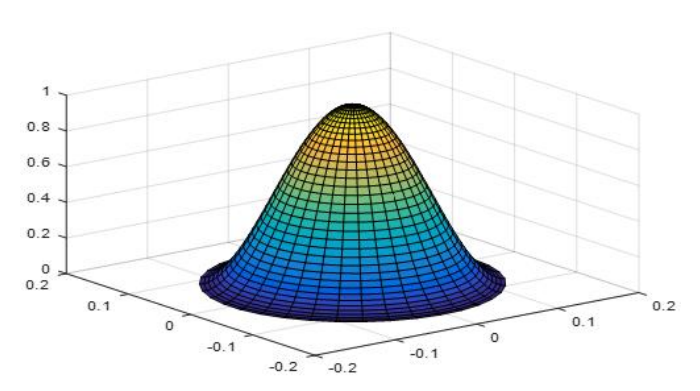


Figure 5. First mode of clamped circular plate corresponding to k = 0, m = 1

2.5 Deriving the damping matrix

By applying the orthogonality conditions for the free vibration mode shape, the proportional damping matrix can be deduced

$$c = m \sum_{i} a_{i} \left[\mathbf{m}^{-1} \quad \mathbf{k} \right]^{j} \tag{17}$$

where, a_j are arbitrary coefficients. By considering many terms of series (17), the proportional damping matrix that gives any desired damping ratios ζ_n at specified frequency ω_n , can be constructed.

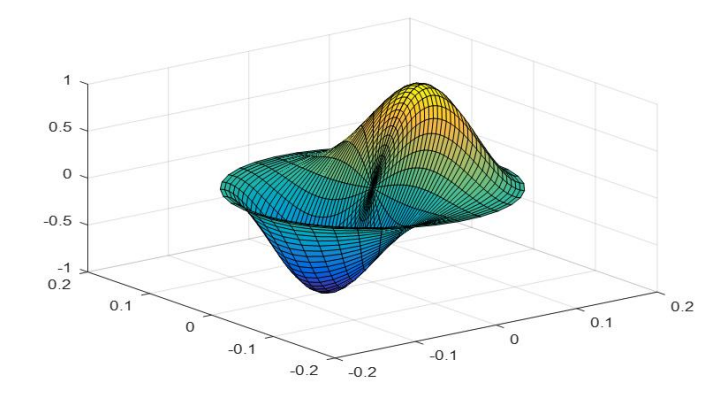


Figure 6. Second mode of clamped circular plate corresponding to k = 1, m = 1

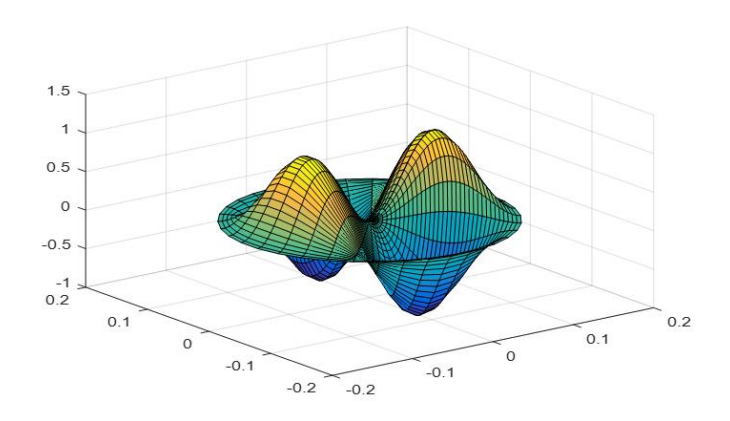


Figure 7. Third mode of clamped circular plate corresponding to k = 2, m = 1

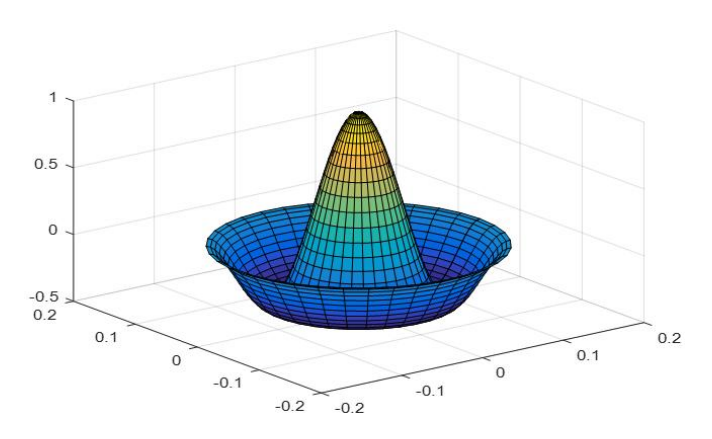


Figure 8. Fourth mode of clamped circular plate corresponding to k = 0, m = 2

To evaluate the constants a_j the following relation can be used

$$\zeta_n = \frac{1}{2\omega_n} \sum_j a_j \omega_n^{2j} \tag{18}$$

where, the values of j can fall anywhere range $-\infty < j < \infty$. It is desirable to select the values of j as close to zero as possible. The details of this derivation can be found in reference [20]. If four specific damping ratios in any four modes have the frequencies ω_m , ω_n , ω_o , ω_p (as in the case), the resulting equations from Eq. (18) are as follows:

$$\begin{pmatrix}
a_{-1} \\ a_0 \\ a_1 \\ a_2
\end{pmatrix} = 2 \begin{bmatrix}
1/\omega_m^2 & 1/\omega_m & \omega_m & \omega_m^3 \\
1/\omega_n^2 & 1/\omega_n & \omega_n & \omega_n^3 \\
1/\omega_o^2 & 1/\omega_o & \omega_o & \omega_o^3 \\
1/\omega_p^2 & 1/\omega_p & \omega_p & \omega_p^3
\end{bmatrix}^{-1} \begin{pmatrix}
\zeta_m \\
\zeta_n \\
\zeta_o \\
\zeta_p
\end{pmatrix}$$
(19)

where, j = -1, 0, +1, and +2 (close to zero) were used.

3. EXPERIMENTAL WORK

Figure 9 shows the experimental setup used to conduct the modal test on solid and perforated circular plates. The modal experimental rig generally consists of two upper and lower rigid steel rings, and the test specimen (circular thin plate) is bolted between them using 12 steel bolts. Four accelerometers, type 4507-B-002, were evenly distributed on the plate to measure the frequency response function FRF. The impact hammer, type 8206, with a steel tip, was used for excitation. All equipment was from Bruel and Kjaer Vibration Instruments Company. Each accelerometer weighs 4.7 g and is assumed to have a negligible mass. When the accelerometers were placed on a plate, the nodal diametric lines and nodal circles were avoided.

The aims of the experiment were (1) To measure the damping ratio ζ_i at the first four natural frequencies, which they used to construct the proportional damping matrix via Eqs. (17)-(19). (2) To verify the feasibility of the theoretical model used to consider the internal plate damping.

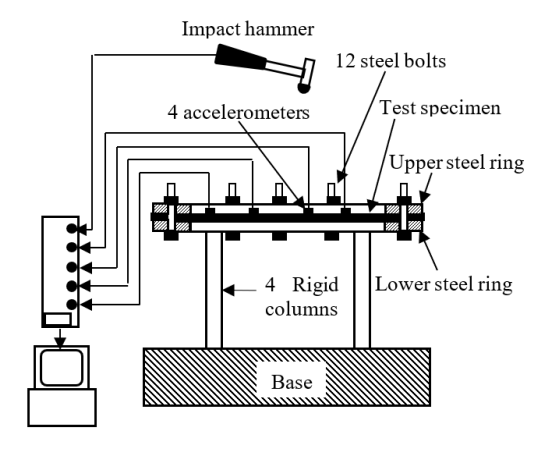


Figure 9. The experimental setup

The FRF was obtained by exciting the position i(i = 1,2,3,4) of the accelerometer and measuring the responses from position (j = 1,2,3,4). The FRF is well known as the ratio of the output response of the structure due to an applied force in the frequency domain, and is a complex-valued number. A peak of the magnitude values of FRF indicates the frequency at the resonance (natural frequency) of the plate.

Figure 10 illustrates the magnitude of the FRF for a plate with a square pattern (η equals 0.75). While the mode shapes of the plate can be extracted experimentally from the imaginary part of the FRF. Figure 11 shows the real and imaginary parts of the FRF for a plate with a square pattern (η equals 0.75). These indicate that the imaginary part corresponding to the first peak (200 Hz) obtained by all accelerometers has the same sign (first mode). On the other hand, the imaginary parts corresponding to the second peak (400 Hz) obtained from the first three accelerometers have a sign opposite to the sign for the fourth one (second mode).

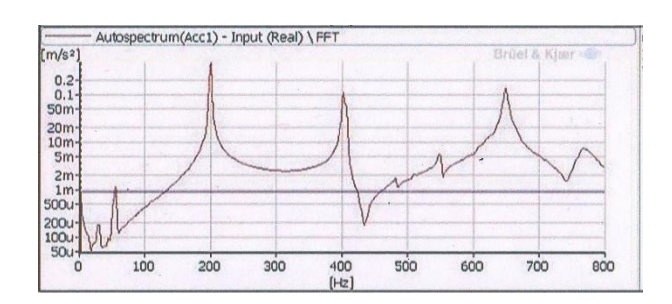


Figure 10. Magnitude of FRF from first accelerometer (For η = 0.75 square pattern)

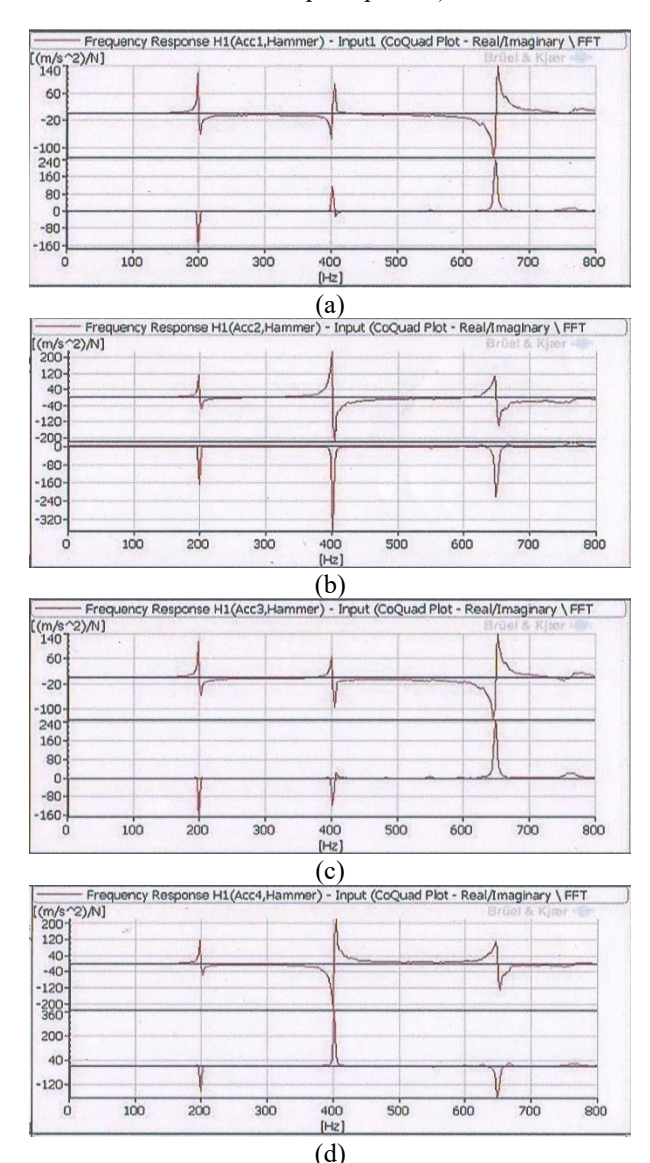


Figure 11. Real and imaginary parts of FRF from four accelerometers (For $\eta = 0.75$ square pattern)

Figure 12 shows the typical FRF magnitude plot versus ω . The peak values of this relation correspond to resonance conditions ($\omega = \omega_i$) where i is the mode number. Two peaks appear in the frequency range in Figure 12.

To determine the modal damping ratio (ζ) experimentally, for *i*-th mode, the quadrature peak picking method was used [21].

$$\zeta_i = \frac{\omega_{bi} - \omega_{ai}}{\omega_i} \tag{20}$$

where, ω_i is the natural frequency at the resonance *i* and ω_{ai} and ω_{hi} satisfy the condition.

$$|FRF(\omega_{ai})| = |FRF(\omega_{bi})| = \frac{|FRF(\omega_i)|}{\sqrt{2}}$$

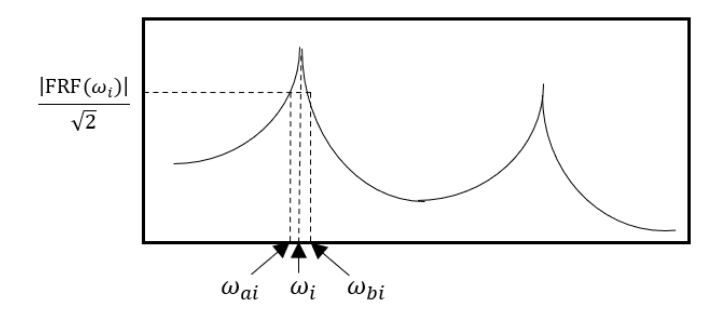


Figure 12. Calculation of the model damping ratio using the quadrature peak picking method

The damping ratios corresponding to the first four natural frequencies of the solid (unperforated) plate are listed in Table 1.

Table 1. Damping ratio corresponding to first four natural frequencies of the solid plate

Mode No.	$\omega_{0,1}$	$\omega_{1,1}$	$\omega_{2,1}$	$\omega_{0,2}$
Damping ratio (ζ)	0.05	0.3	0.27	0.247

In this study, five circular plates (one solid and four perforated) were used in a modal test. The plate's geometric specifications are shown in Table 2.

Table 2. Geometric specifications of five specimens

	Pitch (mm)	Pattern			
Ligament Efficiency (η)		Triangle		Square	
		No. of Holes	Hole Diameter (mm)	No. of Holes	Hole Diameter (mm)
(solid)	-	-	-	-	-
0.75	40	43	10	40	10
0.5	40	37	20	32	20

All the specimens have a thickness of h equals 2 mm and a diameter of 300 mm. The material of plates was mild steel having E = 200 GPa, v = 0.3, and $\rho_p = 7900$ kg·m⁻³.

4. RESULTS AND DISCUSSION

Matlab software was used to perform double integration numerically (Eq. (4)) to evaluate mass and stiffness matrices. The 12 (n = 12) trial comparison function ($W_i(r, \theta)$) is used to evaluate both mass and stiffness matrices, and then the damping matrix. The first four natural frequencies corresponding to mode indices (k,m) = 01, 11, 21, 02 for five cases (one solid two square patterns corresponding to $\eta = 0.75$ and 0.5, and two triangular patterns corresponding to $\eta = 0.75$ and 0.5) were investigated in this study. Figure 13 shows experimental and theoretical values of a circular solid plate's first four natural frequencies. It can be seen from the figure, the differences between experimental and theoretical natural

frequencies are almost negligible. Therefore, it is clear that the eigenfunctions of the solid plate (Eq. (14)) are used as comparison functions in the Galerkin approach is acceptable to describe the dynamic characteristics of a circular plate.

Figures 14-17 show experimental and theoretical values of the first four natural frequencies of square and triangular patterns perforated circular plates. In these figures, the mode numbers 1, 2, 3, and 4 refer to mode indices (k,m) = 01, 11, 21, 02, respectively. All these figures indicate the reduction in the first four natural frequencies as ligament efficiency (η) becomes smaller due to the stiffness dropping more rapidly than mass.

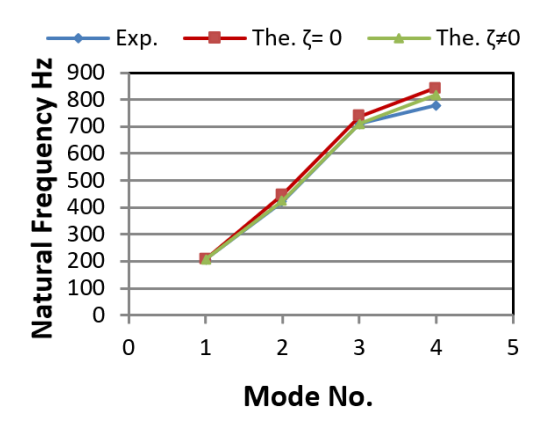


Figure 13. Experimental and theoretical (with and without damping) and experimental results of the first four natural frequencies for a solid plate

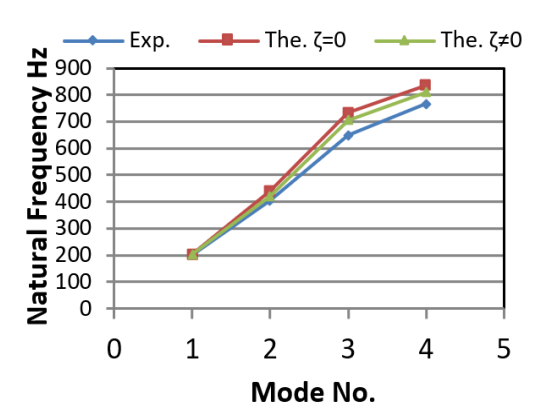


Figure 14. Experimental and theoretical (with and without damping) results of the first four natural frequencies for a square perforated plate ($\eta = 0.75$)

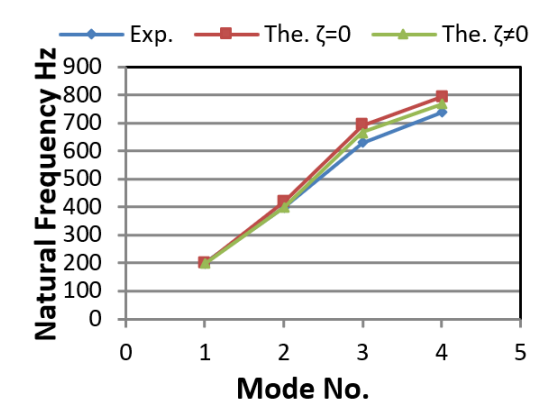


Figure 15. Experimental and theoretical (with and without damping) results of the first four natural frequencies for a square perforated plate ($\eta = 0.5$)

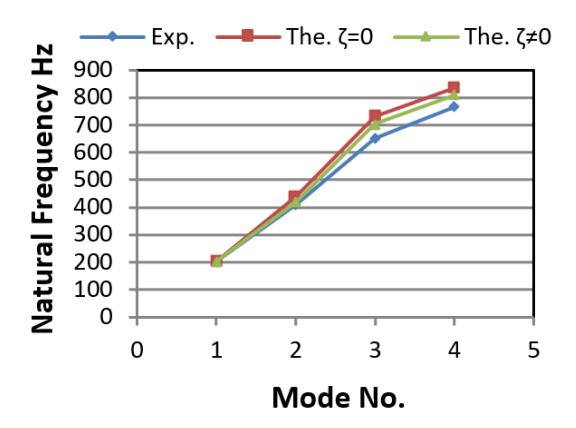


Figure 16. Experimental and theoretical (with and without damping) results of the first four natural frequencies for a triangular perforated plate ($\eta = 0.75$)

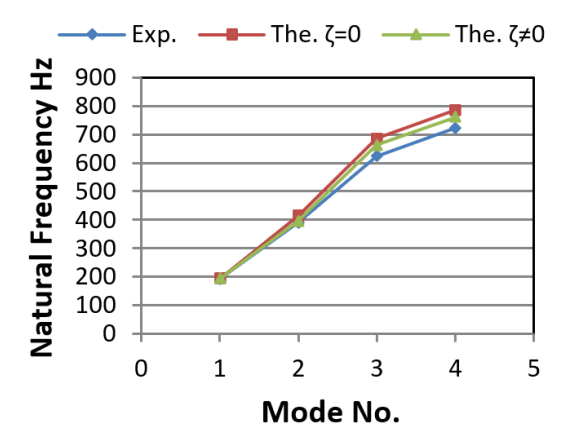


Figure 17. Experimental and theoretical (with and without damping) results of the first four natural frequencies for a triangular perforated plate ($\eta = 0.5$)

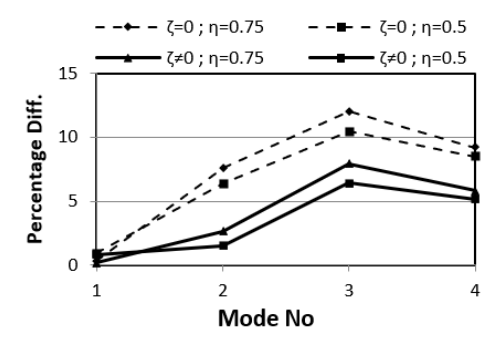


Figure 18. Percentage difference between theoretical and experimental results for triangular penetration

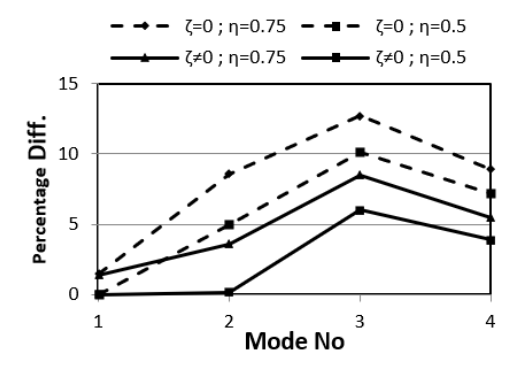


Figure 19. Percentage difference between theoretical and experimental results for square penetration

The effect of internal damping of plate material is also depicted in Figures 14-17. The percentage differences between theoretical and experimental results due to internal damping with mode number are illustrated in Figures 18 and 19 for triangular and square penetration, respectively. As shown in the Figures, the internal damping of plate material significantly reduces the difference between experimental and theoretical results for different penetration patterns and ligament efficiencies.

Numerical values of the drop in percentage difference due to internal damping are listed in Table 3. These values remain almost stable for a certain mode number regardless of the pattern of penetration and ligament efficiency, which are 0.1% for the first mode, 4.9% for the second mode, 4.1% for the third mode and 3.4% for the fourth mode. This indicates that in this study, the perforated circular plate is replaced by a solid circular plate with equivalent stiffness and damping matrices.

The presented approach can be used to study the dynamic characteristics of perforated plates when submerged in fluid, instead of finite element analysis, due to the fine mesh requirement, which is time-consuming.

Table 3. Numerical drops in percentage difference due to equivalent damping matrix

Mada Na	Triangle		Square		
Mode No.	$\eta = 0.75$	$\eta = 0.5$	$\eta = 0.75$	$\eta = 0.5$	
$\omega_{0,1}$	0.13	0.1	0.1	0.0	
$\omega_{1,1}$	5	4.9	5	4.8	
$\omega_{2,1}$	4.1	4.1	4.2	4.1	
$\omega_{0,2}$	3.4	3.4	3.4	3.3	

5. CONCLUSIONS

The internal material damping of a perforated circular plate was taken into account by deriving an equivalent damping matrix. In this study, the perforated circular plate was replaced by a solid one with equivalent stiffness and mass matrices. The proportional damping principle was used to evaluate the damping matrix. The main conclusions of this study can be summarised as follows:

- A good result can be obtained when the eigenfunctions of a solid circular plate (Eq. (14)) are used as a trial function in the Galerkin approach.
- A 12-trial function was adequate in the Galerkin approach to evaluate the mass, stiffness, then damping matrix for circular plates.
- Significant reductions in the percentage difference between theoretical and experimental results were found when internal material damping is taken into account.
- Numerical values of percentage difference reduction between theoretical and experimental results were 0.1% for the first mode, 4.9% for the second mode, 4.1% for the third mode and 3.4% for the fourth mode, regardless of ligament efficiency and type of penetration.

The presented approach needs to be extended to include mixed boundary conditions and to partially perforate circular plates.

ACKNOWLEDGEMENTS

The Vibration Lab, College of Engineering, Tikrit University, Iraq, supports this study's experiments.

REFERENCES

- [1] Erdiwansyah, E., Mahidin, M., Husin, H., Nasaruddin, N., Gani, A. (2023). Effect of modification perforated plate for combustion temperature in fluidized-bed combustor. Mathematical Modelling of Engineering Problems, 10(1): 360-365. https://doi.org/10.18280/mmep.100142
- [2] Mali, K.D., Singru, P.M. (2013). Determination of the fundamental frequency of perforated rectangular plates: Concentrated negative mass approach for the perforation. Advances in Acoustics and Vibration, 2013(1): 972409. https://doi.org/10.1155/2013/972409
- [3] Ismail, A.Y., Noerpamoengkas, A., Zakaria, S.I.F.S. (2018). Effect of micro-holes addition on the natural frequency and mode shape of perforated plates. Journal of Advanced Research in Applied Sciences and Engineering Technology, 11(1): 1-6.
- [4] Cunningham, S.M., Tanner, D.A., Clifford, S., Butan, D., Southern, M. (2020). Effect of perforations on resonant modes of flat circular plates. Key Engineering Materials, 865: 31-35. https://doi.org/10.4028/www.scientific.net/KEM.865.31
- [5] Jamali, H., Mohammed, M.N., Aljibori, H.S.S., Al-Tamimi, A., et al. (2023). Vibration characteristics of perforated plate using experimental and numerical approaches. In 2023 IEEE 8th International Conference on Engineering Technologies and Applied Sciences (ICETAS), Bahrain, Bahrain, pp. 1-4. https://doi.org/10.1109/ICETAS59148.2023.10346538
- [6] Kharchenko, S., Samborski, S., Kharchenko, F., Paśnik, J. (2023). Numerical study of the natural oscillations of perforated vibrating surfaces with holes of complex geometry. Advances in Science and Technology. Research Journal, 17(6): 73-87. http://doi.org/10.12913/22998624/174062
- [7] Zhang, H., Li, Z., Wang, S., Liu, T., Wang, Q. (2024). Analysis of vibration characteristics for rotating braided fiber-reinforced composite annular plates with perforations. Materials, 17(22): 5402. https://doi.org/10.3390/ma17225402
- [8] Prasshanth, C.V., Kumar, A., Lokavarapu, B.R. (2024). Vibration analysis of perforated functionally graded circular plates. Materials Today: Proceedings. https://doi.org/10.1016/j.matpr.2024.04.100
- [9] Slot, T., O'Donnell, W.J. (1971). Effective elastic constants for thick perforated plates with square and triangular penetration patterns. Journal of Manufacturing Science and Engineering, 93(4): 935-942. https://doi.org/10.1115/1.3428087
- [10] O'Donnell, W.J. (1973). Effective elastic constants for the bending of thin perforated plates with triangular and square penetration patterns. Journal of Manufacturing Science and Engineering, 95(1): 121-128. https://doi.org/10.1115/1.3438086
- [11] Park, S., Jeong, K.H., Kim, T.W., Kim, K.S., Park, K.B. (1998). Free vibration analysis of perforated plates using equivalent elastic properties. Nuclear Engineering and Technology, 30(5): 416-423.
- [12] Jhung, M.J., Jo, J.C. (2006). Equivalent material properties of perforated plate with triangular or square penetration pattern for dynamic analysis. Nuclear Engineering and Technology, 38(7): 689-696.
- [13] Jhung, M.J., Jeong, K.H. (2015). Free vibration analysis

- of perforated plate with square penetration pattern using equivalent material properties. Nuclear Engineering and Technology, 47(4): 500-511. https://doi.org/10.1016/j.net.2015.01.012
- [14] Ehrhardt, D.A., Harris, R.B., Allen, M.S. (2014). Numerical and experimental determination of nonlinear normal modes of a circular perforated plate. In Topics in Modal Analysis I, Volume 7: Proceedings of the 32nd IMAC, A Conference and Exposition on Structural Dynamics, Springer, Cham, pp. 239-251. https://doi.org/10.1007/978-3-319-04753-9 25
- [15] Jeong, K.H., Jhung, M.J. (2017). Free vibration analysis of partially perforated circular plates. Procedia Engineering, 199: 182-187. https://doi.org/10.1016/j.proeng.2017.09.230
- [16] Jeong, K.H., Kim, J.M., Ahn, K.H. (2025). Extraction of effective elastic constants of perforated plates with triangular hole pattern using modal analysis. Nuclear Engineering and Technology, 57(10): 103663. https://doi.org/10.1016/j.net.2025.103663
- [17] Ventsel, E., Krauthammer, T., Carrera, E. (2002). Thin plates and shells: Theory, analysis, and applications. Applied Mechanics Reviews, 55: B72-B73. https://doi.org/10.1115/1.1483356
- [18] Chakraverty, S. (2008). Vibration of Plates. CRC Press. https://doi.org/10.1201/9781420053968-3
- [19] Abushilah, S.F., Khalf, A.M. (2024). Computing the modified Bessel function ratio for sine-model circular distributions. Mathematical Modelling of Engineering Problems, 11(1): 192-198. https://doi.org/10.18280/mmep.110121
- [20] Xu, H., Barbič, J. (2017). Example-based damping design. ACM Transactions on Graphics (TOG), 36(4): 1-14. https://doi.org/10.1145/3072959.3073631
- [21] Mevada, H., Patel, D. (2016). Experimental determination of structural damping of different materials. Procedia Engineering, 144: 110-115. https://doi.org/10.1016/j.proeng.2016.05.013

NOMENCLATURE

a

а	plate radius, mm
D	flexural rigidity of the plate, Nm
D^*	equivalent flexural rigidity of the plate, Nm
Ε	modulus of elasticity, GPa
E^*	equivalent modulus of elasticity, GPa
h	plate thickness, mm
J_k	Bessel's function of the first kind of order <i>k</i>
I_k	modified Bessel's function of the first kind of order k
Y_k	Bessel's function of the second kind of order <i>k</i>
K_k	modified Bessel's function of the second kind of
	order k
$W_i(r,\theta)$	i-th trail function
R	radius of holes, mm

Greek symbols

v	Poisson's ratio
$\phi_i(r,\theta)$	i-th weighting function
ω	radial frequency, rad·s-1
$ ho_P$	plate density, kg·m ⁻³
η	ligament efficiency

APPENDICES

Appendix A

This appendix describes the details of the derivation of Eq. (9).

The partial differential equation of the undamped bending vibration of the circular thin plate in polar coordinates can be written as

$$D\nabla^4 w(r,\theta,t) + \rho_P h \ddot{w}(r,\theta,t) = 0 \tag{A1}$$

The eigenvalues of a plate can be deduced as follows: the deflection *w* can be considered to be separable in space and time as:

$$w(r,\theta,t) = W(r,\theta)e^{-j\omega t}$$
 (A2)

Substituting Eq. (A2) into Eq. (A1), the equivalent factorised form is:

$$(\nabla^2 + \beta^2)(\nabla^2 - \beta^2) W(r, \theta) = 0 \tag{A3}$$

where,

$$\beta^4 = \omega^2 \rho_P h / D \tag{A4}$$

and ω is radial frequency.

By separating the function $W(r,\theta)$ into $F(r)G(\theta)$, i.e.:

$$W(r,\theta) = F(r)G(\theta)$$

Eq. (A3) can be written as:

$$\frac{r^2}{F}\frac{d^2F}{dr^2} + \frac{r}{F}\frac{dF}{dr} \mp \beta^2 r^2 = -\frac{1}{G(\theta)}\frac{d^2G}{d\theta^2} = k^2$$
 (A5)

This is two ordinary differential equation:

$$\frac{d^2G(\theta)}{d\theta^2} + k^2G(\theta) = 0 \tag{A6}$$

$$r^{2}\frac{d^{2}F}{dr^{2}} + r\frac{dF}{dr} + (\mp \lambda^{2}r^{2} - k^{2})F = 0$$
 (A7)

The solution of Eq. (A6) is:

$$G(\theta) = A \cos k(\theta - \alpha)$$

where, k is a constant and equal to $(1, 2, \cdots)$, and α can be choosen zero. Since $G(\theta)$ must be periodic with period 2π [14]. So Eq. (A7) can be written as:

$$r^{2}\frac{d^{2}F}{dr^{2}} + r\frac{dF}{dr} + (\mp \beta^{2}r^{2} - k^{2})F = 0$$
 (A8)

The general solution of Eq. (A8) is:

$$F(r) = C_1 J_k(\beta r) + C_2 Y_k(\beta r) + C_3 I_k(\beta r) + C_4 K_k(\beta r)$$
(A9)

where, $J_k(x)$ is the Bessel function of the first kind, $I_k(x)$ is the modified Bessel function of the first kind, $Y_k(x)$ is the Bessel function of the second kind and $K_k(x)$ is the modified Bessel function of the second kind, all the Bessel functions are of order k, while, C_1 , C_2 , C_3 and C_4 are constants.

Since Y_k and K_k have singularities at the origin, which are contradictory to the reality of the vibration of the centre of the plate, $C_2 = C_4 = 0$ have chosen. Thus, Eq. (A9) is reduced to:

$$W(r,\theta) = \left[C_1 I_k(\beta r) + C_3 I_k(\beta r)\right] A \cos k(\theta) \tag{A10}$$

Appendix B

Identities for the Bessel and modified Bessel functions, where ν is the order of Bessel's function and is λ a parameter:

$$J_{\nu}'(\lambda x) = \left[J_{\nu-1}(\lambda x) - \frac{\nu}{\lambda x} J_{\nu}(\lambda x) \right] \lambda \tag{B1}$$

$$I'_{\nu}(\lambda x) = \left[I_{\nu-1}(\lambda x) - \frac{\nu}{\lambda x}I_{\nu}(\lambda x)\right]\lambda \tag{B2}$$

$$J_{-n}(x) = (-1)^n J_{-n}(x)$$
 (B3)

$$I_{-n}(x) = I_n(x) \tag{B4}$$

where, n is an integer.

Appendix C

Derivatives of Bessel's $J_{\nu}(\lambda x)$ and modified Bessel's function $I_{\nu}(\lambda x)$ up to order four:

$$\frac{dJ_{\nu}(\lambda x)}{dx} = \frac{\lambda}{2} \left(J_{\nu-1}(\lambda x) - J_{\nu+1}(\lambda x) \right)$$
 (C1)

$$\frac{d^2 J_{\nu}(\lambda x)}{dx^2} = \left(\frac{\lambda}{2}\right)^2 \left(J_{\nu-2}(\lambda x) - 2J_{\nu}(\lambda x) + J_{\nu+2}(\lambda x)\right)$$
 (C2)

$$\frac{d^{3}J_{\nu}(\lambda x)}{dx^{3}} = \left(\frac{\lambda}{2}\right)^{3} \left(J_{\nu-3}(\lambda x) - 3J_{\nu-1}(\lambda x) + 3J_{\nu+1}(\lambda x) - J_{\nu+3}(\lambda x)\right)$$
(C3)

$$\frac{d^{4}J_{\nu}(\lambda x)}{dx^{3}} = \left(\frac{\lambda}{2}\right)^{4} \left(J_{\nu-4}(\lambda x) - 4J_{\nu-2}(\lambda x) + 6J_{\nu}(\lambda x) - 4J_{\nu+2}(\lambda x) + J_{\nu+4}(\lambda x)\right)$$
(C4)

$$\frac{dI_{\nu}(\lambda x)}{dx} = \frac{\lambda}{2} \left(I_{\nu+1}(\lambda x) + I_{\nu-1}(\lambda x) \right) \tag{C5}$$

$$\frac{d^{2}I_{\nu}(\lambda x)}{dx^{2}} = \left(\frac{\lambda}{2}\right)^{2} \left(I_{\nu+2}(\lambda x) + 2I_{\nu}(\lambda x) + I_{\nu-2}(\lambda x)\right)$$
 (C6)

$$\frac{d^{3}I_{\nu}(\lambda x)}{dx^{3}} = \left(\frac{\lambda}{2}\right)^{3} \left(I_{\nu+3}(\lambda x) + 3I_{\nu+1}(\lambda x) + 3I_{\nu-1}(\lambda x) + I_{\nu-3}(\lambda x)\right)$$
(C7)

$$\frac{d^{4}I_{\nu}(\lambda x)}{dx^{3}} = \left(\frac{\lambda}{2}\right)^{4} \left(I_{\nu+4}(\lambda x) + 4I_{\nu+2}(\lambda x) + 6I_{\nu}(\lambda x) + 4I_{\nu-2}(\lambda x) + I_{\nu-4}(\lambda x)\right)$$
(C8)